43rd AIAA/ASME/SAE/ASEE Joint Propulsion Conference & Exhibit
8 - 11 July 2007, Cincinnati, OH

AIAA 2007-5561

Acoustic Streaming Effects in Liquid Rocket Engines with Transverse Mode Oscillations

Sean R. Fischbach,* Gary A. Flandro† and Joseph Majdalani‡
University of Tennessee Space Institute, Tullahoma, TN 37388

This study considers a simulated liquid rocket engine in which uniform injection is imposed at the faceplate. The corresponding cylindrical chamber has a small length-to-diameter ratio with respect to solid and hybrid rockets. Given their low chamber aspect ratios, liquid thrust engines are known to experience severe tangential and radial oscillation modes more often than longitudinal ones. In order to model this behavior, tangential and radial waves are superimposed onto a basic mean-flow model that consists of a steady, uniform axial velocity throughout the chamber. Considerable effort is given to correctly satisfy the no-slip condition at the chamber's injector face. Sidewall boundary layers that develop at the lateral wall are not considered, being inconsequential to the flow in the vicinity of the headwall. Using perturbation tools, both potential and viscous flow equations are linearized in the pressure wave amplitude and solved to the second order. The effects of the headwall Mach number are leveraged as well. While the potential flow analysis does not predict any acoustic streaming effects, the viscous solution carried out to the second-order approximation gives rise to steady secondary flow patterns near the headwall. These axisymmetric, steady contributions to the tangential and radial traveling waves are induced by the convective flow motion through interactions with inertial and viscous forces. Suppressing either the convective terms or viscosity at the headwall can lead to spurious solutions that are free from streaming. In our problem, streaming is initiated at the headwall, within the boundary layer, and extends throughout the chamber. The present work demonstrates that nonlinear streaming effects of tangential and radial waves inside a cylinder with headwall injection act to alter the outer solution. As a result of streaming, the radial wave velocities are intensified in one half of the domain and reduced in the opposite half at any instant of time. Similarly, the tangential waves are either enhanced or weakened in two opposing sectors that are at 90 degree angle to the radial velocity counterparts. The second-order viscous solution that we obtain clearly displays both an oscillating and a steady flow component. We find that the steady contribution due to streaming can potentially promote the development of large amplitude steepened wave forms. The delineation of this mechanism is crucial for the advancement of analytical tools employed in the prediction of combustion instability. In the present study, streaming is examined in the context of traveling transverse waves. Extending the analysis to standing wave motions can be straightforwardly carried out and will render similar findings.

Nomenclature

a_0 = mean speed of sound
$\boldsymbol{e}_r, \boldsymbol{e}_\theta, \boldsymbol{e}_z$ = unit vectors in r, θ and z directions
f = Hertzian frequency of oscillations, $\omega_0/(2\pi)$
K = dimensionless frequency, $\omega_0 R/a_0$

*Doctoral Research Assistant, Department of Mechanical, Aerospace and Biomedical Engineering. Member AIAA.
†Boling Chair Professor of Excellence in Propulsion, Department of Mechanical, Aerospace and Biomedical Engineering. Associate Fellow AIAA.
‡Jack D. Whitfield Professor of High Speed Flows, Department of Mechanical, Aerospace and Biomedical Engineering. Member AIAA. Fellow ASME.

k_{mn} = wave number for tangential and radial modes m and n
m = tangential oscillation mode shape number
M_b = headwall injection Mach number, V_b / a_0
$\boldsymbol{n}$ = outward pointing unit normal vector
n = radial oscillation mode shape number
p = pressure
r, θ, z = radial, tangential, and axial coordinates
R = chamber radius
t = time
T = temperature
$\boldsymbol{u}$ = total velocity vector
$\boldsymbol{U}$ = mean flow velocity vector
X = rescaled viscous wave number, $X_r + iX_i$

Greek
δ = viscous parameter, $[\nu/(a_0 R)]^{1/2}$
ε = wave amplitude
γ = ratio of specific heats
ν = kinematic viscosity, μ/ρ
ρ = density
ω = unsteady vorticity magnitude
ω_0 = dimensional frequency of oscillations, $2\pi f$
Ω = mean vorticity magnitude
ζ = boundary layer coordinate, $\zeta = z/\delta$

Subscripts
0 = mean flow property
m = mode number
t = partial derivative with respect to time

Superscripts
* = dimensional quantity
r, i = part of a complex variable
' = unsteady flow variable
– = steady flow variable

I. Introduction

THE occurrence of high amplitude pressure oscillations has long been an ailment plaguing large scale combustors. While several investigators in the aero-propulsion industry have been active in modeling and diagnosing this problem in the United States[1-14] and Europe,[15,16] the staggering complexity of the issues confronting modelers often leads to unresolved questions. Acoustic streaming constitutes one such example for which the underpinning physical mechanisms remain unclear. Its origination, manifestation, and influence on wave steepening will be the chief focus of this paper.

Combustion instability in liquid rocket engines is characterized by large amplitude pressure fluctuations, an elevated mean pressure, and frequencies that closely match linear chamber acoustics.[8,9] Owing to this fact, analytical methodologies put forward to describe flow oscillations lean heavily on the assumption of small acoustic disturbances.[14,17] Contrary to this assumption, however, a vast body of experimental evidence conveys a dissimilar picture, specifically one involving large amplitude oscillations with steep gradients in flow variables. For example, in the extensive experimental work of Clayton, Sotter and co-workers,[18-21] a heavily instrumented, laboratory scale, 20,000 lbf thrust engine was used to investigate high amplitude tangential oscillations. Their measurements exhibited sustained, steep-fronted pressure fluctuations with peak-to-peak amplitudes that were an order of magnitude larger than the chamber's operating pressure. The pressure transducers available at the time could not

record data rapidly enough to determine if a true discontinuity was present, but the acquired wave forms displayed large amplitude spikes followed by long shallow low pressure segments.

Theoretical work attributed to Maslen and Moore[22] has convinced many researchers in the combustion stability community that tangential waves cannot steepen as in the case of plane waves. In their 1956 paper, the investigators studied the effects of secondary flows on tangential wave patterns. A circular cylinder with a zero mean flow was utilized to detail the interaction between tangential waves and the chamber's sidewall. Specifically, the secondary flow induced by viscous forces at the sidewall was delineated. Their analysis yielded a streaming profile that acted in the direction opposite to the wave spinning motion. As a result, the investigators determined that steep fronted, shock-like waves could not be produced due to sidewall scattering and viscous dissipation. Later, a study by Flandro[23] that incorporated a mean flow along with mass transpiration from the sidewall predicted a streaming flow in the same direction as the first-order wave. This result was found to be dependent on the magnitude of the injection Mach number. With extensive work already done involving radial boundary layers,[24-29] it is only natural to investigate wave boundary layer interactions in the axial case as well. The motivation to tackle the axial, headwall boundary layer analog is led by experimental results suggesting that the location of the highest amplitudes and therefore most severe waves can be very close to the injector face.[18-21]

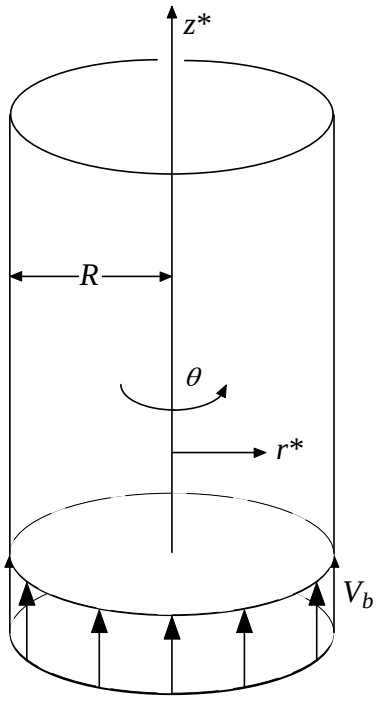

Figure 1. Chamber geometry and coordinate system.

The mechanism that causes a plane wave to steepen is well understood. At the pressure peak the local speed of sound is elevated, thus increasing the local wave propagation rate. At the outset, the crest of the wave overtakes the depressed pressure portion. The curled-up wave continues to steepen until the solution becomes multi-valued when nonlinear forces act to reverse this trend. The present study will demonstrate how streaming flows induced at a liquid engine's injector face can stimulate a similar steepening for tangential waves. In order to model this behavior, tangential and radial waves are superimposed onto a simple mean-flow model. Considerable effort is given to satisfy the no-slip condition at the engine's injector face. The representative geometry, displayed in Fig.1, is that of a semi-infinite cylinder of radius R with a suitable coordinate system anchored at the chamber's headwall. The $z-$coordinate is located along the chamber's centerline.

II. Formulation

For simplicity, we begin the analysis by normalizing all variables according to

$$\begin{cases} p = p^*/P_0 \\ \rho = \rho^*/\rho_0 \end{cases} \quad \begin{cases} \boldsymbol{u} = \boldsymbol{u}^*/a_0 \\ t = t^*/(R/a_0) \end{cases} \quad \begin{cases} r = r^*/R \\ z = z^*/R \end{cases} \quad \begin{cases} T = T^*/T_0 \\ \boldsymbol{\omega} = \boldsymbol{\omega}^*/(a_0/R) \end{cases} \tag{1}$$

The corresponding dimensionless equations written for a viscous compressible fluid consist of

Continuity

$$\frac{\partial \rho}{\partial t} + \nabla \cdot (\rho \boldsymbol{u}) = 0 \tag{2}$$

Momentum

$$\rho\left(\frac{\partial \boldsymbol{u}}{\partial t} + \frac{1}{2}\nabla \boldsymbol{u}^2 - \boldsymbol{u} \times \boldsymbol{\omega}\right) = -\frac{1}{\gamma}\nabla p - \delta^2 \nabla \times (\nabla \times \boldsymbol{u}) + \delta_d^2 \nabla (\nabla \cdot \boldsymbol{u}) + \boldsymbol{F} \tag{3}$$

State

$$p = \rho T \tag{4}$$

The viscous and dilatational parameters that appear in Eq. (3) are defined as

$$\delta^2 = \frac{\nu}{a_0 L} \;\; ; \;\; \delta_d^2 = \left(\frac{\eta}{\mu} + \frac{4}{3} \right) \delta^2 \tag{5}$$

A. Unsteady Flow Equations

Decomposing the flow variables into steady and unsteady parts can be achieved by setting

$$\boldsymbol{u} = M_b \boldsymbol{U} + \boldsymbol{u}' ; \;\; \boldsymbol{\omega} = \bar{\boldsymbol{\Omega}} + \boldsymbol{\omega}' ; \;\; p = \bar{P} + p' ; \;\; \rho = \bar{\rho} + p' ; \;\; T = \bar{T} + T' \tag{6}$$

where overbars denote mean flow properties and primes represent unsteady variables. Substituting Eq. (6) into the governing equations enables us to isolate two sets of steady and unsteady equations. Subsequently, a perturbation expansion may be implemented to linearize the unsteady equations. This is accomplished by expanding each fluctuation a' in terms of a sequence in the pressure wave parameter,

$$a' = \varepsilon a^{(1)} + \varepsilon^2 a^{(2)} + \varepsilon^3 a^{(3)} + ... \tag{7}$$

Here a represents a generic flow variable, and ε is the wave parameter, the ratio of the unsteady pressure amplitude and the mean pressure. Retaining terms to the second order in ε enables us to capture the acoustic streaming effect. As elegantly described by Schlichting[30] (p. 431), the secondary, streaming flow "has its origin in the convective terms and is due to the interaction between inertia and viscosity." Furthermore, "simplifications in which the convective terms have been omitted lead to solutions which are free from streaming and may, therefore, give a misleading representation of the flow. Streaming does, in general, appear only when the solution is carried out to at least the second-order approximation." In this spirit, we perform some algebra and collect the first and second-order sets of equations, specifically

$$\begin{cases} \dfrac{\partial \rho^{(1)}}{\partial t} = -\nabla \cdot \boldsymbol{u}^{(1)} - M_b \nabla \cdot \left[\rho^{(1)} \boldsymbol{U} \right] \\ \dfrac{\partial \boldsymbol{u}^{(1)}}{\partial t} = -\dfrac{\nabla p^{(1)}}{\gamma} - M_b \left[\boldsymbol{u}^{(1)} \cdot \nabla \boldsymbol{U} + \boldsymbol{U} \cdot \nabla \boldsymbol{u}^{(1)} \right] + \boldsymbol{F}^{(1)} - \delta^2 \nabla \times \boldsymbol{\omega}^{(1)} + \delta_d^2 \nabla \left[\nabla \cdot \boldsymbol{u}^{(1)} \right] \\ p^{(1)} = T^{(1)} + \rho^{(1)} \end{cases} \tag{8}$$

and

$$\begin{cases} \dfrac{\partial \rho^{(2)}}{\partial t} = -\nabla \cdot \boldsymbol{u}^{(2)} - \nabla \cdot \left[\rho^{(1)} \boldsymbol{u}^{(1)} \right] - M_b \nabla \cdot \left[\rho^{(2)} \boldsymbol{U} \right] \\ \dfrac{\partial \boldsymbol{u}^{(2)}}{\partial t} = -\dfrac{\nabla p^{(2)}}{\gamma} - M_b \left\{ \boldsymbol{u}^{(2)} \cdot \nabla \boldsymbol{U} + \boldsymbol{U} \cdot \nabla \boldsymbol{u}^{(2)} + \rho^{(1)} \left[\boldsymbol{u}^{(1)} \cdot \nabla \boldsymbol{U} + \boldsymbol{U} \cdot \nabla \boldsymbol{u}^{(1)} \right] \right\} \\ \qquad\qquad - \rho^{(1)} \dfrac{\partial \boldsymbol{u}^{(1)}}{\partial t} - \boldsymbol{u}^{(1)} \cdot \nabla \boldsymbol{u}^{(1)} + \boldsymbol{F}^{(2)} - \delta^2 \nabla \times \boldsymbol{\omega}^{(2)} + \delta_d^2 \nabla \left[\nabla \cdot \boldsymbol{u}^{(2)} \right] \\ p^{(2)} = T^{(2)} + T^{(1)} \rho^{(1)} + \rho^{(2)} \end{cases} \tag{9}$$

B. Headwall Injection Flowfield

It may be instructive to note that Eqs. (8)-(9) represent the interaction equations that prescribe the unsteady wave motion in the simulated liquid rocket thrust engine. Both expressions of conservation of mass and momentum are strongly influenced by the headwall injection Mach number M_b and the mean flowfield function $\boldsymbol{U}$. In the context of a liquid rocket chamber, we recognize that the injection process at the headwall or injector faceplate can be extremely complex. However, we also realize that despite the inherent complexity of the injection patterns, a streamtube motion is quickly established. Bearing these factors in mind, we adopt a simple representation of the mean flowfield that consists of a uniform stream with constant velocity. This basic approximation will be necessary to simplify the problem and, in the process, help to elucidate the underpinning physical mechanisms with minimal algebraic encumbrance. Further complexity can of course be pursued at a later time. It should be kept in mind,

however, that the uniform flow assumption is accompanied by certain limitations; these will be brought to light later in the analysis. With the near injector faceplate as the principal region of interest, we assume steady injection. Recalling that the non-dimensional mean flow is expressed as $\bar{\boldsymbol{U}} = M_b \boldsymbol{U}$, we take

$$\boldsymbol{U} = (0)\boldsymbol{e}_r + (0)\boldsymbol{e}_\theta + (1)\boldsymbol{e}_z \tag{10}$$

This basic representation is illustrated in Fig. 1.

III. Potential Flow Solution

Away from the headwall region, viscous effects are confined to a very thin layer along the lateral, non-injecting sidewall. At the outset, a potential inviscid field may be assumed in the downstream region that is sufficiently removed from the injectors. Such a potential flow representation plays the role of an outer solution with respect to the flow adjacent to the headwall. By discounting viscosity, one is left with a set of wave-like equations that are described next.

A. First-Order Potential Solution

A combination of the first-order momentum and continuity equations delivers an expression for the unsteady wave motion to $\mathcal{O}(\varepsilon)$. In the process, body forces and those associated with two-phase flow interactions are dismissed. The isentropic flow assumption is made, whence the pressure and density are related via

$$\gamma \rho^{(1)} = p^{(1)} \tag{11}$$

As usual, constructing the wave equation requires taking the time derivative of the continuity equation and subtracting from it the divergence of the momentum equation. One readily obtains

$$\nabla^2 p^{(1)} - p_{tt}^{(1)} = -\frac{\partial}{\partial t}\left\{ M_b \nabla \cdot \left[p^{(1)} \boldsymbol{U} \right] \right\} + \gamma M_b \nabla^2 \left[\boldsymbol{U} \cdot \boldsymbol{u}^{(1)} \right] - \gamma M_b \nabla \cdot \left[\boldsymbol{U} \times \boldsymbol{\omega}^{(1)} \right] \tag{12}$$

To represent the oscillatory variables, Euler's notation is used, namely,

$$a' = a e^{-iKt} \tag{13}$$

where $K = \omega_0 R / a_0$ is the dimensionless frequency and ω_0 is the actual radian frequency. Equation (12) becomes

$$\nabla^2 p^{(1)} + K^2 p^{(1)} = iK \left[M_b \boldsymbol{U} \cdot \nabla p^{(1)} \right] + \gamma M_b \nabla^2 \left[\boldsymbol{U} \cdot \boldsymbol{u}^{(1)} \right] - \gamma M_b \nabla \cdot \left[\boldsymbol{U} \times \boldsymbol{\omega}^{(1)} \right] \tag{14}$$

Given that the right-hand-side in the above is of $\mathcal{O}(M_b)$, the first-order pressure can be represented by a dual perturbation expansion in M_b. Thus each level in the pressure wave parameter may be extended successively as

$$a' = \varepsilon \left[a^{(1,0)} + M_b a^{(1,1)} + M_b^2 a^{(1,2)} + \ldots \right] + \varepsilon^2 \left[a^{(2,0)} + M_b a^{(2,1)} + M_b^2 a^{(2,2)} + \ldots \right] + \ldots \tag{15}$$

Subsequent expansions of the first-order wave equation yield

$$\begin{cases} \nabla^2 p^{(1,0)} + K^2 p^{(1,0)} = 0 \\ \boldsymbol{n} \cdot \nabla p^{(1,0)} \Big|_{z=0} = 0; \quad \boldsymbol{n} \cdot \nabla p^{(1,0)} \Big|_{r=1} = 0 \end{cases} \tag{16}$$

$$\begin{cases} \nabla^2 p^{(1,1)} + K^2 p^{(1,1)} = iK \boldsymbol{U} \cdot \nabla p^{(1,0)} + \gamma \nabla^2 \left[\boldsymbol{U} \cdot \boldsymbol{u}^{(1,0)} \right] - \gamma \nabla \cdot \left[\boldsymbol{U} \times \boldsymbol{\omega}^{(1,0)} \right] \\ \boldsymbol{n} \cdot \nabla p^{(1,1)} \Big|_{z=0} = 0; \quad \boldsymbol{n} \cdot \nabla p^{(1,1)} \Big|_{r=1} = 0 \end{cases} \tag{17}$$

and

$$\begin{cases} \nabla^2 p^{(1,2)} + K^2 p^{(1,2)} = iK \boldsymbol{U} \cdot \nabla p^{(1,1)} + \gamma \nabla^2 \left[\boldsymbol{U} \cdot \boldsymbol{u}^{(1,1)} \right] - \gamma \nabla \cdot \left[\boldsymbol{U} \times \boldsymbol{\omega}^{(1,1)} \right] \\ \boldsymbol{n} \cdot \nabla p^{(1,2)} \Big|_{z=0} = 0; \quad \boldsymbol{n} \cdot \nabla p^{(1,2)} \Big|_{r=1} = 0 \end{cases} \tag{18}$$

Note that the appropriate boundary condition forces the pressure gradient to vanish at the chamber surfaces. To solve Eq. (16), separation of variables may be used to derive the first-order pressure in the form of $p^{(1,0)} = F(r)G(\theta)H(z)$. At the outset, the wave equation collapses into

$$\frac{\mathrm{d}^2F}{\mathrm{d}r^2}\frac{1}{R}+\frac{1}{r}\frac{\mathrm{d}F}{\mathrm{d}r}\frac{1}{R}+\frac{1}{r^2}\frac{\mathrm{d}^2G}{\mathrm{d}\theta^2}\frac{1}{G}+K^2=-\frac{\mathrm{d}^2H}{\mathrm{d}z^2}\frac{1}{H}=k_l^2 \tag{19}$$

A solution for $H(z)$ is readily found to be that of a longitudinal wave. In the present work, the longitudinal wave number k_l is set to zero in order to isolate the tangential and radial wave contributions. The left-hand-side of Eq. (19) is manipulated into

$$r^2\frac{\mathrm{d}^2F}{\mathrm{d}r^2}\frac{1}{F}+r\frac{\mathrm{d}F}{\mathrm{d}r}\frac{1}{F}+r^2K^2=-\frac{\mathrm{d}^2G}{\mathrm{d}\theta^2}\frac{1}{G}=m^2 \tag{20}$$

On one hand, knowing that the $\theta-$ dependence cannot be multi-valued, $G(\theta)$ becomes

$$G=A_\theta e^{im\theta} \tag{21}$$

On the other hand, the radial dependence reducesto the standard Bessel equation

$$\frac{\mathrm{d}^2F}{\mathrm{d}r^2}+\frac{1}{r}\frac{\mathrm{d}F}{\mathrm{d}r}+F\left(k_{mn}-\frac{m^2}{r^2}\right)=0 \quad \text{or} \quad F=A_rJ_m(k_{mn}r)+B_rY(k_{mn}r) \tag{22}$$

The byproduct of tangential and radial contributions is hence

$$p^{(1,0)}=AJ_m(k_{mn}r)e^{i(m\theta)}+BY(k_{mn}r)e^{i(m\theta)} \tag{23}$$

Equation (23) must exhibit a finite pressure at the centerline (i.e., $B=0$) and a vanishing pressure gradient at the impermeable sidewall, $J_m'(k_{mn})=0$. Using unit normalization for $p^{(1,0)}$, the first order in ε and zeroth order in M_b approximation for the pressure becomes

$$p^{(1,0)}=\cos(m\theta-Kt)J_m(k_{mn}r);\quad m=0,1,2,\ldots;\quad n=0,1,2,\ldots \tag{24}$$

where k_{mn} is determined by the roots of the first derivative of the Bessel function of order m, $J_m'(k_{mn})=0$. For example, one finds $k_{01}\simeq 3.83170597$, $k_{10}\simeq 1.84118378$, $k_{11}\simeq 5.33144277$, $k_{02}\simeq 7.01558667$, $k_{20}\simeq 3.05423693$, etc. Being chiefly concerned with the effect of tangential wave motion at the headwall, the first spinning mode of interest is k_{10}. Note that Eq. (24) captures both tangential and radial oscillation modes. Using Eqs. (8) and (15) produces a set of equations representing the first-order potential velocity

$$\begin{cases}\dfrac{\partial \boldsymbol{u}^{(1,0)}}{\partial t}=-\dfrac{\nabla p^{(1,0)}}{\gamma}\\ \boldsymbol{n}\cdot\boldsymbol{u}^{(1,0)}\Big|_{z=0}=0;\quad \boldsymbol{n}\cdot\boldsymbol{u}^{(1,0)}\Big|_{r=1}=0\end{cases} \tag{25}$$

$$\begin{cases}\dfrac{\partial \boldsymbol{u}^{(1,1)}}{\partial t}=-\dfrac{\nabla p^{(1,1)}}{\gamma}-\boldsymbol{u}^{(1,0)}\cdot\nabla\boldsymbol{U}-\boldsymbol{U}\cdot\nabla\boldsymbol{u}^{(1,0)}\\ \boldsymbol{n}\cdot\boldsymbol{u}^{(1,1)}\Big|_{z=0}=0;\quad \boldsymbol{n}\cdot\boldsymbol{u}^{(1,1)}\Big|_{r=1}=0\end{cases} \tag{26}$$

and

$$\begin{cases}\dfrac{\partial \boldsymbol{u}^{(1,2)}}{\partial t}=-\dfrac{\nabla p^{(1,2)}}{\gamma}-\boldsymbol{u}^{(1,1)}\cdot\nabla\boldsymbol{U}-\boldsymbol{U}\cdot\nabla\boldsymbol{u}^{(1,1)}\\ \boldsymbol{n}\cdot\boldsymbol{u}^{(1,2)}\Big|_{z=0}=0;\quad \boldsymbol{n}\cdot\boldsymbol{u}^{(1,2)}\Big|_{r=1}=0\end{cases} \tag{27}$$

The first order in ε and zeroth order in M_b inviscid velocity profile may be evaluated to be

$$\boldsymbol{u}^{(1,0)}=\frac{1}{\gamma K}\sin(m\theta-Kt)J_m'(k_{mn}r)\boldsymbol{e}_r+\frac{1}{\gamma K}\left(\frac{m}{r}\right)\cos(m\theta-Kt)J_m(k_{mn}r)\boldsymbol{e}_\theta+(0)\boldsymbol{e}_z \tag{28}$$

By carrying the solution to higher orders in the injection Mach number, the same recursive formulation is obtained at every order. By summing all terms, one deduces

$$\begin{cases} \boldsymbol{u}^{(1)} = \left(\sum_{j=0}^{\infty} M_b^{\,j} \right) \boldsymbol{u}^{(1,0)} = \dfrac{1}{1-M_b} \boldsymbol{u}^{(1,0)} \\ p^{(1)} = \left(\sum_{j=0}^{\infty} M_b^{\,j} \right) p^{(1,0)} = \dfrac{1}{1-M_b} p^{(1,0)} = \dfrac{J_m\left(k_{mn} r\right)}{1-M_b} \cos\left(m\theta - Kt\right) \end{cases} \tag{29}$$

Note that the infinite series are reducible by use of the identity

$$\sum_{j=0}^{\infty} x^j = \frac{1}{1-x} \tag{30}$$

By summing over an infinite series in the Mach number, the solution is captured exactly in M_b, specifically with a truncation error equal to

$$\lim_{j \to \infty} M_b^{\,j} = 0. \tag{31}$$

Therefore, for the remainder of the analysis, the highly accurate solution will be represented through the use of $\boldsymbol{u}^{(1)}$ and $p^{(1)}$.

B. Second-Order Potential Solution

The second-order wave equation can be retrieved at $\mathcal{O}(\varepsilon^2)$, with the outcome being

$$\nabla^2 p^{(2)} - p_{tt}^{\,(2)} = \frac{1-\gamma}{2\gamma} \left\{ \left[p^{(1)} \right]^2 \right\}_{tt} + \nabla \cdot p_t^{(1)} \boldsymbol{u}^{(1)} - \frac{\gamma \nabla^2}{2} \left[\boldsymbol{u}^{(1)} \cdot \boldsymbol{u}^{(1)} \right] + M_b \left[\nabla \cdot p^{(2)} U \right]_t - \gamma M_b \nabla \cdot \left\{ \nabla \left[\boldsymbol{U} \cdot \boldsymbol{u}^{(2)} \right] - \boldsymbol{U} \times \boldsymbol{\omega}^{(2)} \right\} \tag{32}$$

Parallel expansion in the Mach number can be performed using

$$p^{(2)} = p^{(2,0)} + M_b p^{(2,1)} + M_b^2 p^{(2,2)} + \ldots \tag{33}$$

This enables us to extract, at leading order in the Mach number and second order in the wave amplitude,

$$\begin{cases} \nabla^2 p^{(2,0)} - p_{tt}^{\,(2,0)} = \dfrac{1-\gamma}{2\gamma} \left\{ \left[p^{(1,0)} \right]^2 \right\}_{tt} + \nabla \cdot \left[p_t^{(1,0)} \boldsymbol{u}^{(1,0)} \right] - \dfrac{\gamma}{2} \nabla^2 \left[\boldsymbol{u}^{(1,0)} \cdot \boldsymbol{u}^{(1,0)} \right] \\ \boldsymbol{n} \cdot \nabla p^{(2,0)} \Big|_{z=0} = 0; \quad \boldsymbol{n} \cdot \nabla p^{(2,0)} \Big|_{r=1} = 0 \end{cases} \tag{34}$$

Inserting the first-order flowfield on the right-hand-side gives

$$\nabla^2 p^{(2,0)} - p_{tt}^{(2,0)} = F(r) + B(r) \cos\left[2\left(m\theta - Kt\right) \right] \tag{35}$$

where

$$F(r) = \frac{1}{2\gamma K^2} \left[\begin{array}{l} \left(\dfrac{3m^2}{r^3} + \dfrac{K^2}{r} \right) J_m\left(k_{mn} r\right) J_m'\left(k_{mn} r\right) + \left(K^2 - \dfrac{m^2}{r^2} \right) J_m'^2\left(k_{mn} r\right) + \left(K^2 - \dfrac{m^2}{r^2} \right) J_m\left(k_{mn} r\right) J_m''\left(k_{mn} r\right) \\ -\dfrac{1}{r} J_m'\left(k_{mn} r\right) J_m''\left(k_{mn} r\right) - J_m''^2\left(k_{mn} r\right) - J_m'\left(k_{mn} r\right) J_m'''\left(k_{mn} r\right) - \dfrac{2m^2}{r^4} J_m^2\left(k_{mn} r\right) \end{array} \right] \tag{36}$$

and

$$B(r) = \frac{1}{2\gamma K^2} \left\{ \begin{array}{l} 2\left[K^4\left(\gamma - 1\right) + \dfrac{K^2 m^2}{r^2} - \dfrac{m^2\left(1-m^2\right)}{r^4} \right] J_m^2\left(k_{mn} r\right) + J_m''^2\left(k_{mn} r\right) \\ -\left(\dfrac{K^2}{r} - \dfrac{3m^2}{r^3} \right) J_m\left(k_{mn} r\right) J_m'\left(k_{mn} r\right) - \left(K^2 + \dfrac{3m^2}{r^2} \right) J_m'^2\left(k_{mn} r\right) \\ -\left(K^2 + \dfrac{m^2}{r^2} \right) J_m\left(k_{mn} r\right) J_m''\left(k_{mn} r\right) + \dfrac{J_m'\left(k_{mn} r\right) J_m''\left(k_{mn} r\right)}{r} + J_m'\left(k_{mn} r\right) J_m'''\left(k_{mn} r\right) \end{array} \right\} \tag{37}$$

As in the previous section, the wave equation is further expanded in terms of the injection Mach number. The approximation to the set of second-order equations displays a pattern that is of familiar type. We find

$$p^{(2)} = \sum_{n=0}^{\infty} M_b^n \left[(n+1)\, p_p^{(2,0)} + \cos(m\theta - Kt)\, J_m(k_{mn} r) \right] = \frac{p^{(2,0)} + (1-M_b)\cos(m\theta - Kt)\, J_m(k_{mn} r)}{(1-M_b)^2} \tag{38}$$

where the particular solution $p_p^{(2,0)}$ is given by

$$p_p^{(2,0)} = H(r) + G(r)\cos\left[2(m\theta - Kt)\right] \tag{39}$$

with

$$H(r) = -\frac{1}{4\gamma K^2}\left\{\left[\left(\frac{m}{r}\right)^2 - K^2\right] J_m(k_{mn} r)^2 + J_m'(k_{mn} r)^2\right\} \tag{40}$$

and

$$\begin{cases} G(r) = \dfrac{1}{4\gamma K^2}\left[-\left(\dfrac{m^2}{r^2} + 3K^2\right) J_m(k_{mn} r)^2 + J_m'(k_{mn} r)^2 + 4K^4(\gamma - 1)\, f(r)\right]; \\ f'' + \dfrac{1}{r} f' - 4\left(\dfrac{m^2}{r^2} - K^2\right) f = J_m(k_{mn} r)^2 \end{cases} \tag{41}$$

The second-order momentum equation may be expanded along similar lines. One gets

$$\boldsymbol{u}^{(2)} = \sum_{j=0}^{\infty} M_b^j \left[(n+1)\, \boldsymbol{u}_p^{(2,0)} + \boldsymbol{u}^{(1,0)} \right] = \frac{(1-M_b)\, \boldsymbol{u}^{(1,0)} + \boldsymbol{u}^{(2,0)}}{(1-M_b)^2} \tag{42}$$

where

$$\boldsymbol{u}_p^{(2,0)} = \begin{cases} -\dfrac{1}{2\gamma^2 K}\left[2 J_m(k_{mn}) J_m'(k_{mn} r) + (1-\gamma) K^2 f'(r)\right] \sin\left[2(m\theta - Kt)\right] \boldsymbol{e}_r \\ -\dfrac{1}{\gamma^2 K}\left(\dfrac{m}{r}\right)\left[J_m^2(k_{mn} r) + K^2(1-\gamma)\, f(r)\right] \cos\left[2(m\theta - Kt)\right] \boldsymbol{e}_\theta \\ +(0)\, \boldsymbol{e}_z \end{cases} \tag{43}$$

Unlike the second-order pressure $p^{(2)}$, the velocity in Eq. (43) does not exhibit a steady, second-order streaming component. It may be worthwhile to mention that in other streaming studies,[30-32] one may see both steady and unsteady second-order contributions to the velocity. In such models, the second order pressure gradient is assumed or even ignored. In the present study, the use of such an assumption is not required. Instead, we recall Schlichting's[30] description (p. 430), namely, that "a potential flow which is periodic with respect to time induces a steady, secondary ('streaming') motion … as a result of viscous forces." In this vein, we realize that a viscous model must be pursued in order to suitably capture the second-order interactions, as attempted in similar context by Maslen and Moore.[22]

IV. Viscous Flow

Attention is now turned to the region directly above the headwall, specifically to the viscous boundary layer that must develop as a result of transverse shear parallel to the injector faceplate. This boundary layer is necessary to bring the transverse components of the velocity, both tangential and radial, to vanish at the surface. Friction at the headwall permits the attainment of a more realistic representation of the fluid motion. The ensuing flowfield must, on the one hand, satisfy the no slip condition at the headwall and, on the other hand, merge with the outer solution in the farfield. In the present study, we ignore the sidewall boundary layers and assume that all viscous effects are contained within a small region near the headwall.

A. First-Order Viscous Solution

In our attempt to unravel the acoustic streaming motion induced by viscous effects at the injector faceplate, the boundary layer equations at the headwall must be established. Following standard perturbation practices, a coordinate transformation is introduced such that the z-coordinate is rescaled over the viscous thickness δ. The corresponding inner, slow variable becomes

$$\zeta = \frac{z}{\delta} \tag{44}$$

Expanding the first-order momentum equation in terms of ζ leads to a set of three linear second-order partial differential equations (PDEs). These are

$$\begin{cases} -iKu_r^{(1)} = -\dfrac{M_b}{\delta}\dfrac{\partial u_r^{(1)}}{\partial \zeta} - \dfrac{1}{\gamma}\dfrac{\partial p^{(1)}}{\partial r} + \dfrac{\partial^2 u_r^{(1)}}{\partial \zeta^2} \\ -iKu_\theta^{(1)} = -\dfrac{M_b}{\delta}\dfrac{\partial u_\theta^{(1)}}{\partial \zeta} - \dfrac{1}{\gamma r}\dfrac{\partial p^{(1)}}{\partial \theta} + \dfrac{\partial^2 u_\theta^{(1)}}{\partial \zeta^2} \\ -iKu_z^{(1)} = -\dfrac{M_b}{\delta}\dfrac{\partial u_z^{(1)}}{\partial \zeta} - \dfrac{1}{\gamma \delta}\dfrac{\partial p^{(1)}}{\partial z} + \dfrac{\delta_d^2}{\delta^2}\dfrac{\partial^2 u_z^{(1)}}{\partial \zeta^2} \end{cases} \tag{45}$$

Tangential Solution:

To illustrate the procedural steps, we start with the tangential equation

$$\frac{\partial^2 u_\theta^{(1)}}{\partial \zeta^2} - \frac{M_b}{\delta}\frac{\partial u_\theta^{(1)}}{\partial \zeta} + iKu_\theta^{(1)} = \frac{1}{\gamma r}\frac{\partial p^{(1)}}{\partial \theta} \tag{46}$$

Owing to the fact that M_b / δ is not small, all terms on the left-hand-side of Eq. (46) are of order unity. Using the outer pressure from the potential flowfield to represent $p^{(1)}$, one collects

$$\frac{\partial^2 u_\theta^{(1)}}{\partial \zeta^2} - \frac{M_b}{\delta}\frac{\partial u_\theta^{(1)}}{\partial \zeta} + iKu_\theta^{(1)} = \frac{i}{\gamma}\left(\frac{m}{r}\right)\frac{J_m\left(k_{mn} r\right)}{\left(1 - M_b\right)} e^{i(m\theta - Kt)} \tag{47}$$

The particular integral for Eq. (47) may be readily evaluated such that a compact solution is deduced. One gets

$$\left[u_\theta^{(1)}\right]_p = \frac{1}{\gamma K}\left(\frac{m}{r}\right)\frac{J_m\left(k_{mn} r\right)}{\left(1 - M_b\right)} e^{i(m\theta - Kt)} \tag{48}$$

In turn, the homogenous solution takes the form

$$\left[u_\theta^{(1)}\right]_h = A_\theta\left(r, \theta, t\right) e^{X_1 \zeta} + B_\theta\left(r, \theta, t\right) e^{X_2 \zeta} \tag{49}$$

with

$$\left(X_1, X_2\right) = \frac{M_b}{2\delta}\left(1 \pm \sqrt{1 - 4iK\delta^2 M_b^{-2}}\right) = \frac{V_b}{2}\sqrt{\frac{R}{a_0 \nu}}\left(1 \pm \sqrt{1 - 4iK\delta^2 M_b^{-2}}\right)$$

or

$$X_1 = \frac{M_b}{2\delta}\left(1 + \sqrt{\frac{1 + \sqrt{1 + 16K^2\delta^4 M_b^{-4}}}{2}} - i\sqrt{\frac{-1 + \sqrt{1 + 16K^2\delta^4 M_b^{-4}}}{2}}\right) \tag{50}$$

$$X_2 = \frac{M_b}{2\delta}\left(1 - \sqrt{\frac{1 + \sqrt{1 + 16K^2\delta^4 M_b^{-4}}}{2}} + i\sqrt{\frac{-1 + \sqrt{1 + 16K^2\delta^4 M_b^{-4}}}{2}}\right) \tag{51}$$

Note that $X_1 > 0$ and $X_2 < 0$. The total solution for the first-order boundary layer approximation becomes

$$u_\theta^{(1)} = A_\theta\left(r, \theta, t\right) e^{X_1 \zeta} + B_\theta\left(r, \theta, t\right) e^{X_2 \zeta} + \frac{1}{\gamma K}\left(\frac{m}{r}\right)\frac{J_m\left(k_{mn} r\right)}{\left(1 - M_b\right)} e^{i(m\theta - Kt)} \tag{52}$$

Knowing that the velocity cannot increase unboundedly as $\zeta \to \infty$, one must set $A_\theta\left(r, \theta, t\right) = 0$. This leaves the second constant in Eq. (52) to satisfy the no slip condition at the headwall. Subsequently, one puts

$$u_\theta^{(1)}\left(r,\theta,0,t\right)=B_\theta\left(r,\theta,t\right)+\frac{1}{\gamma K}\left(\frac{m}{r}\right)\frac{J_m\left(k_{mn}r\right)}{\left(1-M_b\right)}e^{i(m\theta-Kt)}=0 \tag{53}$$

whence

$$B_\theta\left(r,\theta,t\right)=-\frac{1}{\gamma K}\left(\frac{m}{r}\right)\frac{J_m\left(k_{mn}r\right)}{\left(1-M_b\right)}e^{i(m\theta-Kt)} \tag{54}$$

and so

$$u_\theta^{(1)}(r,\theta,\zeta,t)=\frac{1}{\gamma K}\left(\frac{m}{r}\right)\frac{J_m\left(k_{mn}r\right)}{\left(1-M_b\right)}e^{i(m\theta-Kt)}\left(1-e^{X_2\zeta}\right) \tag{55}$$

It may be useful to remark that $u_\theta^{(1)}(1,\theta,\zeta,t)\neq 0$. The radial velocity fluctuation does not observe the velocity adherence condition at the sidewall. As stated earlier, this outcome is due to our deliberate dismissal of the sidewall boundary layer.

Radial Solution:

In the radial direction, Eq. (45) yields

$$\frac{\partial^2 u_r^{(1)}}{\partial\zeta^2}-\frac{M_b}{\delta}\frac{\partial u_r^{(1)}}{\partial\zeta}+iKu_r^{(1)}=\frac{1}{\gamma}\frac{\partial p^{(1)}}{\partial r} \tag{56}$$

Substituting the pressure from the outer potential flow solution, we get

$$\frac{\partial^2 u_r^{(1)}}{\partial\zeta^2}-\frac{M_b}{\delta}\frac{\partial u_r^{(1)}}{\partial\zeta}+iKu_r^{(1)}=\frac{1}{\gamma}\frac{J_m'\left(k_{mn}r\right)}{\left(1-M_b\right)}e^{i(m\theta-Kt)} \tag{57}$$

The particular integral delivers

$$\left[u_r^{(1)}\right]_p=-\frac{i}{\gamma K}\frac{J_m'\left(k_{mn}r\right)}{\left(1-M_b\right)}e^{i(m\theta-Kt)} \tag{58}$$

with the homogenous solution being of the form

$$\left[u_r^{(1)}\right]_h=A_r\left(r,\theta,t\right)e^{X_1\zeta}+B_r\left(r,\theta,t\right)e^{X_2\zeta} \tag{59}$$

Here one must set $A_r\left(r,\theta,t\right)=0$ to prevent unboundedness in the downstream direction. The complete solution for the first-order radial velocity approximation is therefore

$$u_r^{(1)}=B_r\left(r,\theta,t\right)e^{X_2\zeta}-\frac{i}{\gamma K}\frac{J_m'\left(k_{mn}r\right)}{\left(1-M_b\right)}e^{i(m\theta-Kt)} \tag{60}$$

The no slip condition at the headwall permits extracting the final unknown

$$u_r^{(1)}\left(r,\theta,0,t\right)=B_r\left(r,\theta,t\right)-\frac{i}{\gamma K}\frac{J_m'\left(k_{mn}r\right)}{\left(1-M_b\right)}e^{i(m\theta-Kt)}=0 \quad \text{or} \quad B_r\left(r,\theta,t\right)=\frac{i}{\gamma K}\frac{J_m'\left(k_{mn}r\right)}{\left(1-M_b\right)}e^{i(m\theta-Kt)} \tag{61}$$

Backward substitution yields, at length

$$u_r^{(1)}(r,\theta,\zeta,t)=\frac{i}{\gamma K}\frac{J_m'\left(k_{mn}r\right)}{\left(1-M_b\right)}e^{i(m\theta-Kt)}\left(e^{X_2\zeta}-1\right) \tag{62}$$

Axial Solution:

The continuity equation can be used to extract the z component of velocity to the first order. Inserting $\gamma\rho^{(1)}=p^{(1)}$ into the first-order continuity expression in Eq. (8), one obtains

$$\frac{\partial\rho^{(1)}}{\partial t}=-\nabla\cdot\boldsymbol{u}^{(1)}-M_b\nabla\cdot\left[\rho^{(1)}\boldsymbol{U}\right] \quad \text{or} \quad \frac{\partial p^{(1)}}{\partial t}=-\gamma\nabla\cdot\boldsymbol{u}^{(1)}-\gamma M_b\nabla\cdot\left[\frac{p^{(1)}}{\gamma}\boldsymbol{U}\right]=-\gamma\nabla\cdot\boldsymbol{u}^{(1)}-\cancel{M_b\boldsymbol{U}\cdot\nabla p^{(1)}}=-\gamma\nabla\cdot\boldsymbol{u}^{(1)} \tag{63}$$

In terms of the slow boundary layer coordinate, one can put

$$i\frac{K}{\gamma}p^{(1)} = \frac{\partial u_r^{(1)}}{\partial r} + \frac{u_r^{(1)}}{r} + \frac{1}{r}\frac{\partial u_\theta^{(1)}}{\partial \theta} + \frac{1}{\delta}\frac{\partial u_z^{(1)}}{\partial \zeta} \tag{64}$$

Substituting Eqs. (29), (55), and (62) into Eq. (64), one can rearrange and retrieve

$$\frac{\gamma}{\delta}\frac{\partial u_z}{\partial \zeta} = -\frac{ie^{i(m\theta - Kt)}}{K(1-M_b)}\left\{\left[J_m''(k_{mn}r) + \frac{1}{r}J_m'(k_{mn}r) - \frac{m^2}{r^2}J_m(k_{mn}r)\right]\left(e^{X_2\zeta} - 1\right) - K^2 J_m(k_{mn}r)\right\} \tag{65}$$

Noting that, by definition, $J_m(k_{mn}r)$ satisfies the Bessel equation,

$$J_m''(k_{mn}r) + \frac{1}{r}J_m'(k_{mn}r) - \frac{m^2}{r^2}J_m(k_{mn}r) + K^2 J_m(k_{mn}r) = 0 \tag{66}$$

Equation (65) becomes

$$\frac{\partial u_z}{\partial \zeta} = \frac{i\delta K e^{i(m\theta - Kt)}}{\gamma(1-M_b)}J_m(k_{mn}r)e^{X_2\zeta} \tag{67}$$

Subsequent integration yields

$$u_z^{(1)}(r,\theta,\zeta,t) = \frac{i\delta K e^{i(m\theta - Kt)}}{\gamma X_2(1-M_b)}J_m(k_{mn}r)e^{X_2\zeta} + A_z(r,\theta,t) \tag{68}$$

Based on strictly steady axial injection at the headwall, the z-component of velocity must not interfere with the uniform injection at $z = \zeta = 0$. This condition translates into

$$u_z^{(1)}(r,\theta,0,t) = \frac{i\delta K e^{i(m\theta - Kt)}}{\gamma X_2(1-M_b)}J_m(k_{mn}r) + A_z(r,\theta,t) = 0 \quad \text{or} \quad A_z(r,\theta,t) = -\frac{i\delta K e^{i(m\theta - Kt)}}{\gamma X_2(1-M_b)}J_m(k_{mn}r) \tag{69}$$

In the end, one obtains

$$u_z^{(1)} = \frac{i\delta K e^{i(m\theta - Kt)}}{\gamma X_2(1-M_b)}J_m(k_{mn}r)\left(e^{X_2\zeta} - 1\right) \tag{70}$$

The real parts of the solution can be summarized as

$$\boldsymbol{u}^{(1)}(r,\theta,\zeta,t) = \frac{J_m(k_{mn}r)}{\gamma K(1-M_b)}\left\{\begin{aligned}&\frac{J_m'(k_{mn}r)}{J_m(k_{mn}r)}\left[\underbrace{\sin(m\theta - Kt)}_{\text{inviscid outer field}} - \underbrace{\overbrace{\sin\left(m\theta + X_i\,\zeta - Kt\right)}^{\text{rotational part}}\underbrace{e^{X_r\zeta}}_{\text{decay}}}_{\text{wave propagation}}\right]\boldsymbol{e}_r \\ &+\left(\frac{m}{r}\right)\left[\cos(m\theta - Kt) - \cos\left(m\theta + X_i\,\zeta - Kt\right)e^{X_r\zeta}\right]\boldsymbol{e}_\theta \\ &+\frac{\delta K^2}{X_r^2 + X_i^2}\left\{\begin{aligned}&X_r\left[\sin(m\theta - Kt) - e^{X_r\zeta}\sin\left(m\theta + X_i\,\zeta - Kt\right)\right] \\ &+X_i\left[\cos(m\theta - Kt) - e^{X_r\zeta}\cos\left(m\theta + X_i\,\zeta - Kt\right)\right]\end{aligned}\right\}\boldsymbol{e}_z\end{aligned}\right. \tag{71}$$

where $X_2 = X = X_r + iX_i$ may be synthesized from

$$\left\{\begin{aligned}X_r &= \frac{M_b}{2\delta}\left(1 - \sqrt{\frac{1+\sqrt{1+16K^2\delta^4 M_b^{-4}}}{2}}\right) \approx \frac{M_b}{2\delta}\left(1 - \sqrt{1+4K^2\delta^4 M_b^{-4}}\right) \approx -\frac{\delta^3 K^2}{M_b^3} = -\frac{\delta}{S_p} \\ X_i &= \frac{M_b}{2\delta}\sqrt{\frac{\sqrt{1+16K^2\delta^4 M_b^{-4}} - 1}{2}} \approx \frac{M_b}{2\delta}\sqrt{\frac{8K^2\delta^4 M_b^{-4}}{2}} \approx \frac{\delta K}{M_b} = \delta S\end{aligned}\right. \tag{72}$$

It may be useful to remark that the tangential component of the velocity does not vanish at the sidewall. Its behavior in the vicinity of $r = 1$ deteriorates to the extent of overshooting the expected value in the absence of fluid friction at the sidewall. Our domain of analysis is therefore limited to a large diameter chamber with the exclusion of the sidewall. Such a model may be deemed acceptable considering that the principal objective here lies in the treatment of the mean flow interactions with the wave motion directly above the headwall. To illustrate the solution that we

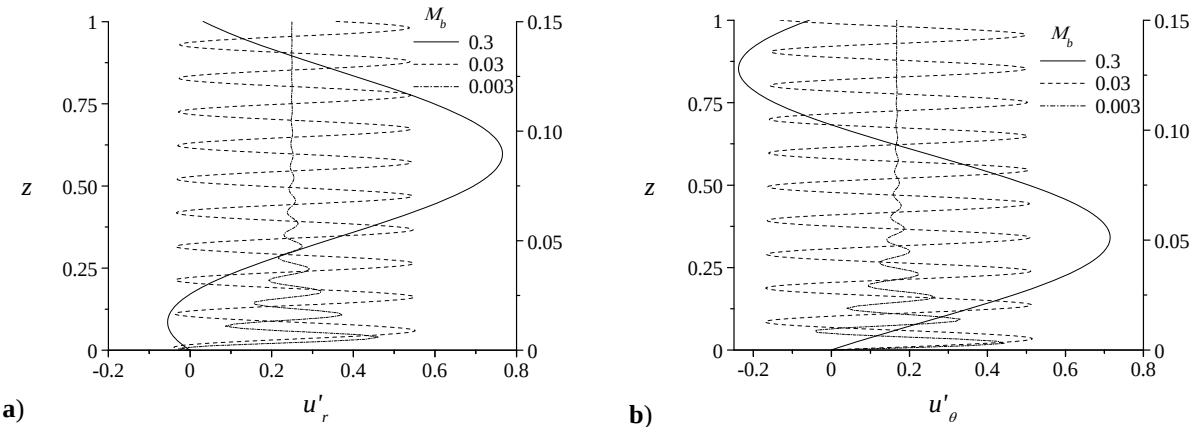

Figure 2. First-order approximations for a) radial and b) tangential velocities. The scale on the left-hand-side is for injection Mach numbers of 0.3 and 0.03. The scale on the right-hand-side is for M_b = 0.003.

obtain, Fig. 2 is used to display the first-order boundary layer approximation for the traveling wave at $r = 0.4$, $\theta = \pi/3$, and $\delta = 0.000647$. The wave evolutions in the streamwise direction are shown at three headwall injection Mach numbers and the first spinning mode number $k_{10} \simeq 1.84118378$. The axial velocity fluctuation is not shown due to its small relative magnitude. It is apparent that the viscous stresses have a more pronounced effect as the injection Mach number is decreased. Conversely, when the injection Mach number is increased, the boundary layer is more effectively blown off the surface (see Cole and Aroesty[33] and Majdalani[24,27]). Furthermore, the propagation wavelength measured by the peak-to-peak distance decreases as the Mach number is lowered. In this case, the decay of the wave is also seen to be more rapid. Physically, this behavior may be attributed to the increased dimensionless frequency, or Strouhal number, given by $S = K/M_b = \omega_0 R/V_b$. As the dimensionless frequency is increased (or the Mach number is decreased), the transverse fluctuations undergo a larger number of reversals per unit time. In the presence of viscosity, the higher frequency at which oscillations occur enhances the effects of fluid friction. Mathematically, the same behavior may be extrapolated from the dependence of the exponential decay terms on M_b. As one may infer from Eq. (72), increasing the Mach number leads to a smaller X_r and, consequently, to a slower viscous damping in the axial direction. In actuality, the net damping is dominated by

$$\exp\left(X_r \zeta\right) \approx \exp\left(-\frac{\delta^2 K^2}{M_b^3} z\right) = \exp\left(-\frac{z}{S_p}\right) \tag{73}$$

where the effective penetration number S_p emerges in the form

$$S_p = \frac{M_b^3}{\delta^2 K^2} = \frac{V_b^3}{a_0^3}\frac{a_0 R}{\nu}\frac{a_0^2}{\omega_0^2 R^2} = \frac{V_b^3}{\nu \omega_0^2 R} \tag{74}$$

This parameter first appears in work by Majdalani[24] and then by Flandro,[6] both in the context of an oscillating longitudinal wave over an injecting surface in a porous cylinder. The penetration number is further explored in porous cylinders[25-28] and channels[34-37] with various injection patterns. In the present study, a similar dimensionless group is found to control the depth of penetration of the headwall boundary layer. This can be clearly seen by letting $\varphi = m\theta - Kt$ and recasting Eq. (71) into

$$\boldsymbol{u}^{(1)} = \frac{1}{\gamma K\left(1-M_b\right)}\Bigg(J_m'\left(k_{mn} r\right)\Big[\sin\varphi - \sin\left(\varphi + Sz\right)e^{-z/S_p}\Big]\boldsymbol{e}_r + \frac{m J_m\left(k_{mn} r\right)}{r}\Big[\cos\varphi - \cos\left(\varphi + Sz\right)e^{-z/S_p}\Big]\boldsymbol{e}_\theta$$

$$+ \frac{K^2 J_m\left(k_{mn} r\right)}{S^2 + S_p^2}\Big\{S\cos\varphi - S_p\sin\varphi + \Big[S_p\sin\left(\varphi + Sz\right) - S\cos\left(\varphi + Sz\right)\Big]e^{-z/S_p}\Big\}\boldsymbol{e}_z\Bigg) \tag{75}$$

Note that as S_p is increased, a larger depth of penetration is realized. Conversely, for small penetration numbers, the exponential damping constant in Eq. (73) will be relatively large, leading to rapid spatial damping of the wave envelope and a shorter penetration depth. Physically, the penetration number unraveled here renders visible the

balance between two co-existing forces: unsteady inertia and the viscous diffusion of the tangential (or radial) velocity in the axial direction. This dimensionless parameter reflects the ratio of

$$\frac{\text{unsteady inertial force}}{\text{viscous force}} \approx \frac{\dfrac{\partial u_\theta^*}{\partial t^*}}{\nu \dfrac{\partial^2 u_\theta^*}{\partial z^{*2}}} \approx \frac{\dfrac{\bar{u}_\theta^*}{\bar{t}^*}}{\nu \dfrac{\bar{u}_\theta^*}{\bar{z}^{*2}}} = \frac{\bar{z}^{*2}}{\nu \bar{t}^*} \approx \frac{(V_b/\omega_0)^2}{\nu (R/V_b)} = \frac{V_b^3}{\nu \omega_0^2 R} = S_p \tag{76}$$

In the above, we use $\bar{z}^* \approx V_b/\omega_0$ to represent the lengthscale of a wave of frequency ω_0 being convected at an axial speed that is proportional to V_b. We also take $\bar{t}^* \approx R/V_b$ to denote the timescale of a particle crossing the radius of the chamber at a characteristic speed equal to V_b. It is clear that the penetration number not only accounts for the influence of inertia and viscosity, but also embodies the effects of mean flow convection in the axial direction. The analogy with the former work on longitudinal waves is significant. While Majdalani and Flandro[28] considered an oscillating axial flow with steady radial mass flux at the porous sidewall, the present study addresses the motion of an oscillating transverse flow with steady axial flux at the headwall. By comparing these two problems, the blowing velocity V_b that appears in Eq. (74) will refer to either the transverse or axial mean flow values at the porous wall. The frequency of oscillations for a given mode shape will also be distinctly different, namely

$$\omega_0 = \begin{cases} \dfrac{k_{mn} a_0}{R} & \text{transverse wave} \\ m \dfrac{\pi a_0}{L} & \text{axial wave} \end{cases} \tag{77}$$

Aside from the blowing velocity and dimensional frequency, the remaining parameters in Eq. (74) are the same in both models. At the outset, a full characterization of the headwall boundary layer may be systematically carried out using the steps delineated by Majdalani.[27] While such analysis may be useful in elucidating the structure of the transverse waves under different oscillatory mode configurations, our attention here remains focused on the streaming effects produced by these waves. To this end, a higher approximation is in order.

B. Second-Order Viscous Solution

In what follows, we show that extending the boundary layer analysis to the second order in the wave parameter gives rise to a steady flow component that has its origin in the interaction between viscosity and inertia. To this end, the second-order momentum equation, defined in Eq. (9), is recast using the stretched inner coordinate ζ. Projecting the result in all three vector directions gives

$$\begin{aligned} \frac{\partial u_r^{(2)}}{\partial t} = &-\frac{M_b}{\delta}\frac{\partial u_r^{(2)}}{\partial \zeta} - \frac{1}{\gamma}\frac{\partial p^{(2)}}{\partial r} - \frac{p^{(1)}}{\gamma}\left[\frac{M_b}{\delta}\frac{\partial u_r^{(1)}}{\partial \zeta} + \frac{\partial u_r^{(1)}}{\partial t}\right] - \left\{\frac{u_z^{(1)}}{\delta}\frac{\partial u_r^{(1)}}{\partial \zeta} + u_r^{(1)}\frac{\partial u_r^{(1)}}{\partial r} + \frac{u_\theta^{(1)}}{r}\left[\frac{\partial u_r^{(1)}}{\partial \theta} - u_\theta^{(1)}\right]\right\} \\ &-\delta^2\left\{\frac{1}{r}\left[\frac{\partial^2 u_\theta^{(2)}}{\partial \theta \partial r} + \frac{1}{r}\frac{\partial u_\theta^{(2)}}{\partial \theta} - \frac{1}{r}\frac{\partial^2 u_r^{(2)}}{\partial \theta^2}\right] - \frac{1}{\delta}\left[\frac{1}{\delta}\frac{\partial^2 u_r^{(2)}}{\partial \zeta^2} - \frac{\partial^2 u_z^{(2)}}{\partial \zeta \partial r}\right]\right\} \\ &+\delta_d^2\left[\frac{\partial^2 u_r^{(2)}}{\partial r^2} + \frac{1}{r}\frac{\partial u_r^{(2)}}{\partial r} - \frac{u_r^{(2)}}{r^2} - \frac{1}{r^2}\frac{\partial u_\theta^{(2)}}{\partial \theta} + \frac{1}{r}\frac{\partial^2 u_\theta^{(2)}}{\partial r \partial \theta} + \frac{1}{\delta}\frac{\partial^2 u_z^{(2)}}{\partial r \partial \zeta}\right] \end{aligned} \tag{78}$$

$$\begin{aligned} \frac{\partial u_\theta^{(2)}}{\partial t} = &-\frac{M_b}{\delta}\frac{\partial u_\theta^{(2)}}{\partial \zeta} - \frac{1}{\gamma r}\frac{\partial p^{(2)}}{\partial \theta} - \frac{p^{(1)}}{\gamma}\left[\frac{M_b}{\delta}\frac{\partial u_\theta^{(1)}}{\partial \zeta} + \frac{\partial u_\theta^{(1)}}{\partial t}\right] - \left[\frac{u_z^{(1)}}{\delta}\frac{\partial u_\theta^{(1)}}{\partial \zeta} + \frac{u_\theta^{(1)}}{r}\frac{\partial u_\theta^{(1)}}{\partial \theta} + u_r^{(1)}\left(\frac{u_\theta^{(1)}}{r} + \frac{\partial u_\theta^{(1)}}{\partial r}\right)\right] \\ &-\delta^2\left\{\frac{1}{\delta}\left[\frac{1}{r}\frac{\partial^2 u_z^{(2)}}{\partial \zeta \partial \theta} - \frac{1}{\delta}\frac{\partial^2 u_\theta^{(2)}}{\partial \zeta^2}\right] - \left[\frac{\partial^2 u_\theta^{(2)}}{\partial r^2} - \frac{u_\theta^{(2)}}{r^2} + \frac{1}{r}\frac{\partial u_\theta^{(2)}}{\partial r} - \frac{1}{r}\frac{\partial^2 u_r^{(2)}}{\partial r \partial \theta}\right]\right\} \\ &+\delta_d^2\left[\frac{1}{r}\frac{\partial^2 u_r^{(2)}}{\partial \theta \partial r} + \frac{1}{r^2}\frac{\partial u_r^{(2)}}{\partial \theta} + \frac{1}{r^2}\frac{\partial^2 u_\theta^{(2)}}{\partial \theta^2} + \frac{1}{r\delta}\frac{\partial^2 u_z^{(2)}}{\partial \theta \partial \zeta}\right] \end{aligned} \tag{79}$$

$$\frac{\partial u_z^{(2)}}{\partial t} = -\frac{M_b}{\delta}\frac{\partial u_z^{(2)}}{\partial \zeta} - \frac{1}{\gamma\delta}\frac{\partial p^{(2)}}{\partial \zeta} - \frac{p^{(1)}}{\gamma}\left[\frac{M_b}{\delta}\frac{\partial u_z^{(1)}}{\partial \zeta} + \frac{\partial u_z^{(1)}}{\partial t}\right] - \left[\frac{u_z^{(1)}}{\delta}\frac{\partial u_z^{(1)}}{\partial \zeta} + u_r^{(1)}\frac{\partial u_z^{(1)}}{\partial r} + \frac{u_\theta^{(1)}}{r}\frac{\partial u_z^{(1)}}{\partial \theta}\right]$$
$$-\frac{\delta^2}{r}\left\{\left[\frac{1}{\delta}\frac{\partial u_r^{(2)}}{\partial \zeta} + \frac{r}{\delta}\frac{\partial^2 u_r^{(2)}}{\partial r\,\partial \zeta} - \frac{\partial u_z^{(2)}}{\partial r} - \frac{\partial^2 u_z^{(2)}}{\partial r^2}\right] - \left[\frac{1}{r}\frac{\partial^2 u_z^{(2)}}{\partial \theta^2} - \frac{1}{\delta}\frac{\partial^2 u_\theta^{(2)}}{\partial \theta\,\partial \zeta}\right]\right\}$$
$$+\delta_d^2\left[\frac{1}{\delta}\frac{\partial^2 u_r^{(2)}}{\partial \zeta\,\partial r} + \frac{1}{r\delta}\frac{\partial u_r^{(2)}}{\partial \zeta} + \frac{1}{r\,\delta}\frac{\partial^2 u_\theta^{(2)}}{\partial \zeta\,\partial \theta} + \frac{1}{\delta^2}\frac{\partial^2 u_z^{(2)}}{\partial \zeta^2}\right] \tag{80}$$

Retaining terms of the zeroth order in δ yields

$$\begin{cases}
\dfrac{\partial^2 u_r^{(2)}}{\partial \zeta^2} - \dfrac{M_b}{\delta}\dfrac{\partial u_r^{(2)}}{\partial \zeta} - \dfrac{\partial u_r^{(2)}}{\partial t} = \dfrac{1}{\gamma}\dfrac{\partial p^{(2)}}{\partial r} + \dfrac{p^{(1)}}{\gamma}\left[\dfrac{M_b}{\delta}\dfrac{\partial u_r^{(1)}}{\partial \zeta} + \dfrac{\partial u_r^{(1)}}{\partial t}\right] + \left[\dfrac{u_z^{(1)}}{\delta}\dfrac{\partial u_r^{(1)}}{\partial \zeta} + u_r^{(1)}\dfrac{\partial u_r^{(1)}}{\partial r} + \dfrac{u_\theta^{(1)}}{r}\left(\dfrac{\partial u_r^{(1)}}{\partial \theta} - u_\theta^{(1)}\right)\right] \\
\dfrac{\partial^2 u_\theta^{(2)}}{\partial \zeta^2} - \dfrac{M_b}{\delta}\dfrac{\partial u_\theta^{(2)}}{\partial \zeta} - \dfrac{\partial u_\theta^{(2)}}{\partial t} = \dfrac{1}{\gamma r}\dfrac{\partial p^{(2)}}{\partial \theta} + \dfrac{p^{(1)}}{\gamma}\left[\dfrac{M_b}{\delta}\dfrac{\partial u_\theta^{(1)}}{\partial \zeta} + \dfrac{\partial u_\theta^{(1)}}{\partial t}\right] + \left[\dfrac{u_z^{(1)}}{\delta}\dfrac{\partial u_\theta^{(1)}}{\partial \zeta} + \dfrac{u_\theta^{(1)}}{r}\dfrac{\partial u_\theta^{(1)}}{\partial \theta} + u_r^{(1)}\left(\dfrac{u_\theta^{(1)}}{r} + \dfrac{\partial u_\theta^{(1)}}{\partial r}\right)\right] \\
\dfrac{\delta_d^2}{\delta^2}\dfrac{\partial^2 u_z^{(2)}}{\partial \zeta^2} - \dfrac{M_b}{\delta}\dfrac{\partial u_z^{(2)}}{\partial \zeta} - \dfrac{\partial u_z^{(2)}}{\partial t} = \dfrac{1}{\gamma\delta}\dfrac{\partial p^{(2)}}{\partial \zeta} + \dfrac{p^{(1)}}{\gamma}\left[\dfrac{M_b}{\delta}\dfrac{\partial u_z^{(1)}}{\partial \zeta} + \dfrac{\partial u_z^{(1)}}{\partial t}\right] + \left[\dfrac{u_z^{(1)}}{\delta}\dfrac{\partial u_z^{(1)}}{\partial \zeta} + \dfrac{u_\theta^{(1)}}{r}\dfrac{\partial u_z^{(1)}}{\partial \theta} + u_r^{(1)}\dfrac{\partial u_z^{(1)}}{\partial r}\right]
\end{cases} \tag{81}$$

where terms involving the ratio M_b/δ will prove to be crucial. Solving the second-order equations requires greater algebraic detail. To briefly sketch the process, the solution in the radial direction is outlined. After substituting the first-order solution on the right-hand-side of Eq. (81), one recovers, for the steady part,

$$\frac{\partial^2 u_r^{(2)}}{\partial \zeta^2} - \frac{M_b}{\delta}\frac{\partial u_r^{(2)}}{\partial \zeta} = \frac{1}{2\gamma^2 K^2\left(1-M_b\right)^2}\left\{\left[\left(\tfrac{m^2}{r^2} + K^2\right)J_m J_m' - \tfrac{m^2}{r^3}J_m^2 + J_m' J_m''\right]e^{2X_r\zeta}\right.$$
$$\left.+\left[2\tfrac{m^2}{r^3}J_m^2 - \left(2\tfrac{m^2}{r^2} + \tfrac{M_b K}{\delta}X_i\right)J_m J_m' - 2J_m' J_m''\right]e^{X_r\zeta}\cos\left(X_i\,\zeta\right) - \tfrac{M_b K}{\delta}J_m J_m' X_r e^{X_r\zeta}\sin\left(X_i\,\zeta\right)\right\} \tag{82}$$

Note that Eq. (82) is a second-order linear PDE that is subject to

$$u_r^{(2)}\left(r,\theta,0\right) = 0; \quad u_r^{(2)}\left(r,\theta,\infty\right) = \text{finite} \tag{83}$$

A straightforward solution may be obtained using the method of undetermined coefficients. The time-independent

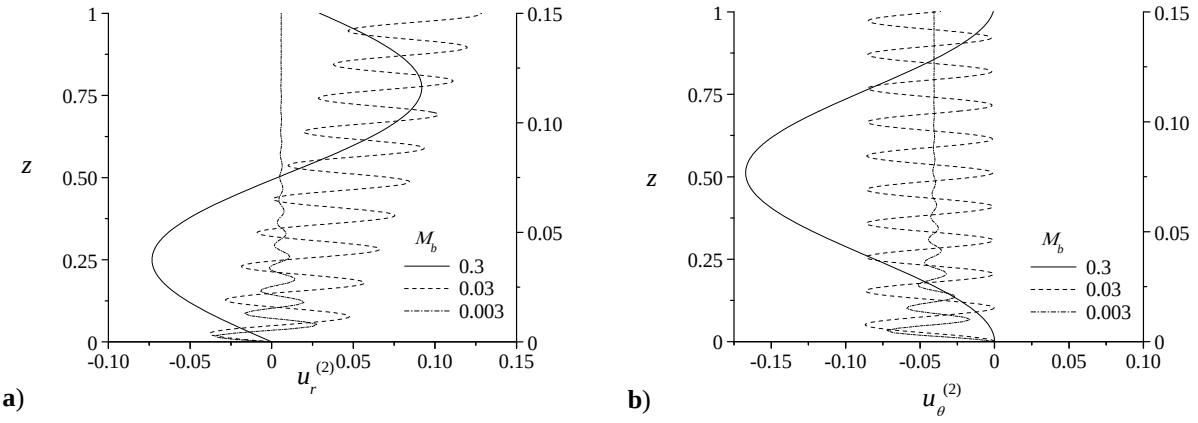

Figure 3. Steady second-order approximations for a) radial and b) tangential velocities. The scale on the left-hand-side is for injection Mach numbers of 0.3 and 0.03. The scale on the right-hand-side is for M_b = 0.003.

result is

$$u_r^{(2)} = \frac{1}{2\gamma^2 K^2 \left(1-M_b\right)^2}\left\{\frac{1}{2X_r\left(2X_r - \frac{M_b}{\delta}\right)}\left[\left(\frac{m^2}{r^2}+K^2\right)J_m J_m' - \frac{m^2}{r^3}J_m^2 + J_m' J_m''\right]\left(e^{2X_r\zeta}-1\right)\right.$$

$$\left. + \Lambda_{r,1}\left[e^{X_r\zeta}\sin\left(X_i\,\zeta\right)\right] + \Lambda_{r,2}\left[e^{X_r\zeta}\cos\left(X_i\,\zeta\right)-1\right]\right\} \tag{84}$$

where

$$\begin{cases} \Lambda_{r,1} = \dfrac{1}{\beta_r}\left\{\begin{array}{l}\left[X_r\left(M_b-\delta X_r\right)-\delta^2 X_i^2\right]\dfrac{m^2}{r^3}J_m^2 + KM_b\left(X_i^3 + X_r X_i\right)J_m J' \\ +\left[\delta^2 X_i^2 + \delta X_r\left(M_b-\delta X_r\right)\right]\left(\dfrac{m^2}{r^2}J_m J' + J_m' J''\right)\end{array}\right\} \\ \Lambda_{r,2} = \dfrac{1}{\beta_r}\left\{\begin{array}{l}\delta X_i\left(M_b-2\delta X_r\right)\left(J_m' J'' - \dfrac{m^2}{r^3}J_m^2\right) + \delta K M_b\left(X_r^2+X_i^2\right)X_i\,J_m J' \\ +\left[\dfrac{m^2}{r^2}\delta X_i\left(M_b-2\delta X_r\right) + KM_b\left(M_b-\delta X_r\right)\left(X_r^2+X_i^2\right)\right]J_m J_m'\end{array}\right\} \end{cases} \tag{85}$$

and

$$\begin{cases} \beta_r = \left(X_r^2 + X_i^2\right)\beta_\theta \\ \beta_\theta = \delta^2 X_i^2 + \left(M_b - \delta X_r\right)^2 \end{cases} \tag{86}$$

In like manner, the steady streaming velocity in the tangential direction may be extracted from Eq. (81). One gets

$$u_\theta^{(2)} = \frac{1}{2\gamma^2 K^2\left(1-M_b\right)^2}\frac{M_b}{\beta_\theta}\left(\frac{m}{r}\right)J_m^2\left\{\left(M_b-\delta X_r\right)\left[e^{X_r\zeta}\cos\left(X_i\,\zeta\right)-1\right] - X_i\,e^{X_r\zeta}\sin\left(X_i\,\zeta\right)\right\} \tag{87}$$

Note that in Eqs. (82)-(87), the abbreviated function J_m stands for $J_m\left(k_{mn}r\right)$; its primes denote derivatives with respect to the radial coordinate. Figure 3 displays the second-order radial and tangential velocities at $r = 0.4$, $\theta = \frac{1}{3}\pi$, and $\delta = 0.000647$ versus the axial coordinate at three headwall injection Mach numbers. The radial velocity exhibits an interesting trend displaying alternating spatial excursions that shift outwardly toward increasingly more positive values. This behavior is most apparent in the case of $M_b = 0.03$ (dashed line in Fig. 3a) where the radial velocity starts vascillating around $u_r \approx 0.005$ and then $u_r \approx 0.075$ in the short span of $z = [0,1]$. The same pattern is repeated in the cases of $M_b = 0.3$ and 0.003, but the positively shifting excursions are masked in the corresponding graphs by the relative scales. These particular trends suggest that when fluid particles convect downstream, away from the injector face, the second-order flowfield becomes increasingly influenced by a steady radial velocity that pushes the fluctuations outwardly toward the sidewall.

In order to compare the first and second-order boundary layer flows, it may be useful to consider the entire wave structure in one particular instant of time. Figures 4 and 5 are snapshots of vector fields representing the first tangential mode of oscillation for the first and second-order solutions, respectively, taken at fixed $z = 0.01, t = 1$ and $\delta = 0.000647$. In Fig. 5, only the steady portion of the second-order solution is shown. Note that the first-order solution in Fig. 4 spins in a counterclockwise fashion as a consequence of the convention assumed in the exponential time dependence. The vector traces shown here have comparable patterns that are merely reoriented in the polar plane with successive decreases in the headwall injection Mach number. Velocity vectors moving from one nodal point to the other are identified in all three plots. These patterns are in sharp contrast to the second-order results shown in Fig. 5, where the velocity vectors display distinctly dissimilar motions. In the cases of $M_b = 0.3$ and 0.03, the flow pattern is dominated by an inward pointing radial velocity drawing mass toward the chamber's centerline with a slight clockwise swirl velocity that is noticeable in the $M_b = 0.03$ case. At first glance, this pattern would appear to retard the first-order motion whose wave structure rotates in a counterclockwise direction.

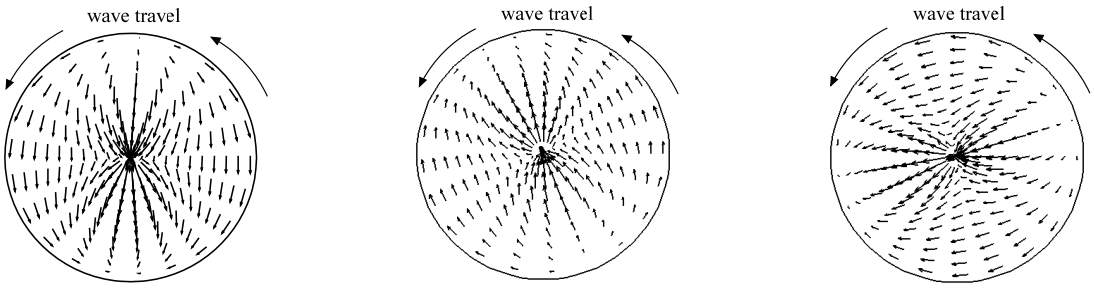

a) **b)** **c)**

Figure 4. First-order traveling wave vector plot at z = 0.01 and three headwall injection Mach numbers of a) M_b = 0.3, b) 0.03, and c) 0.003.

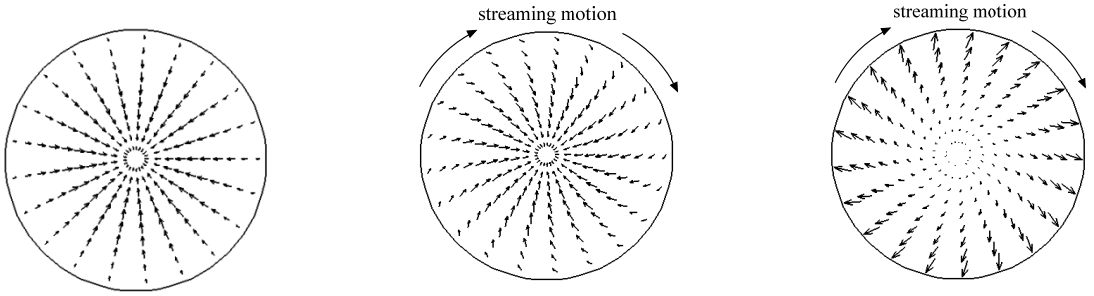

a) **b)** **c)**

Figure 5. Steady second-order velocity vector plot at z = 0.01 and three headwall injection Mach numbers of a) M_b = 0.3, b) 0.03, and c) 0.003.

Although a similar conclusion is reported by Maslen and Moore,[22] a closer examination of the flow behavior suggests the contrary. Note that Fig. 5c displays a strong outward pointing radial velocity with a similar counterclockwise swirl velocity. The disparity between Figs. 5a, 5b and 5c beckons a closer look at Fig. 3. In plotting the second-order radial component, it is seen that the velocity near the headwall fluctuates between positive and negative quantities. At $z = 0.01$, deep within the boundary layer, the two larger injection Mach number cases fall in a negative u_r swing, whereas the smallest Mach number case falls in a positive swing. The corresponding arrowheads are inward pointing in Figs. 5a and 5b but outward in Fig. 5c. However, outside the boundary layer, the arrowheads are always outward pointing as corroborated by the outer limit for $u^{(2)}$, namely, the induced streaming solution.

It should be recalled that streaming flows are normally associated with a second-order steady rotational flow that is independent of viscosity. To extract these terms from the second-order flow solution, the limit is taken as the boundary layer coordinate approaches infinity. One obtains

$$\bar{u}_r^{(2)} = \lim_{\zeta\to\infty} u_r^{(2)} = \frac{-1}{2X_r\left(2X_r - M_b/\delta\right)}\left(\frac{1}{2\gamma^2K^2\left(1-M_b\right)^2}\right)\left[\left(\frac{m^2}{r^2}+K^2\right)J_mJ_m' - \frac{m^2}{r^3}J_m^2 + J_m'J_m''\right] - \frac{\Lambda_{r,2}}{2K^2\gamma^2} \quad (88)$$

$$\bar{u}_\theta^{(2)} = \lim_{\zeta\to\infty} u_\theta^{(2)} = -\frac{1}{2\gamma^2K^2\left(1-M_b\right)^2}\frac{M_b}{\beta_\theta}\left(\frac{m}{r}\right)J_m^2\left(M_b - \delta X_r\right) \quad (89)$$

Reflected in Eqs. (88) and (89) is a second-order steady flow that is deprived of viscous damping terms. Streaming flow investigators often refer to solutions similar to these limiting expressions as second-order "potential" solutions, although they are not totally independent of viscosity.

To illustrate the impact of the streaming solution restored in the outer limit, $\bar{u}_r^{(2)}$ and $\bar{u}_\theta^{(2)}$, on the total potential flow solution, Fig. 6 is used to display vector plots of the second-order approximation first without streaming (a), and then with streaming and either (b) $\delta = 0.00647$ or (c) $\delta = 0.0647$. All results are shown at $\varepsilon = 0.1$, $M_b = 0.3$, $t = 1$, $m = 1$, and $n = 0$ (first order tangential and zeroth order radial). In Fig. 6a, only the total potential flow is depicted to second order. The results are found to be nearly identical to the first-order potential solution and to the patterns in Fig. 4 where the first-order viscous solution is shown. This agreement reflects the diminutive nature of the second-order potential flow contribution. When streaming effects are accounted for, Figs. 6b and 6c bring into perspective the behavior of the total potential flow (to second order) combined with the streaming velocities, $\bar{u}_r^{(2)}$ and $\bar{u}_\theta^{(2)}$. It is quite evident in Fig. 6b that, when we use a typical value of $\delta = 0.00647$, the streaming motion can markedly alter the fundamental flow structure observed in Figs. 4 and 6a. The velocity vectors are pushed outwardly in all directions with the effect being most pronounced in the area around the nodal line where the potential flow vectors are mostly radial. The flow patterns in Figs. 4 and 6a comprise two regions with respect to the axis of rotation, an upstream region where the flow is directed toward the core, and a downstream region where the flow is outward. With the superposition of the streaming correction in Fig. 6b, a reversal in the direction of flow upstream of the centerline may be noted. This flow reversal may be attributed to the large streaming amplitude

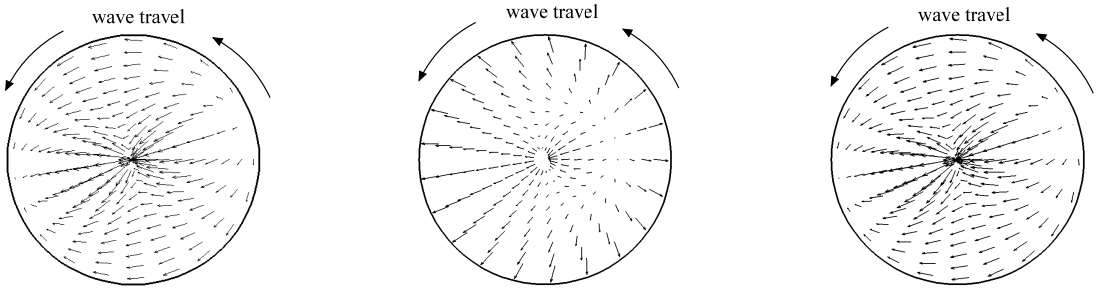

Figure 6. Total vector plot in the outer region illustrating the behavior of a) the purely inviscid potential approximation up to the second order and b-c) the same total potential solution augmented by the streaming contribution. Results are shown for t = 1, n = 1, ε = 0.1, M_b = 0.3 and δ = 0 (a), 0.00647 (b), and 0.0647 (c).

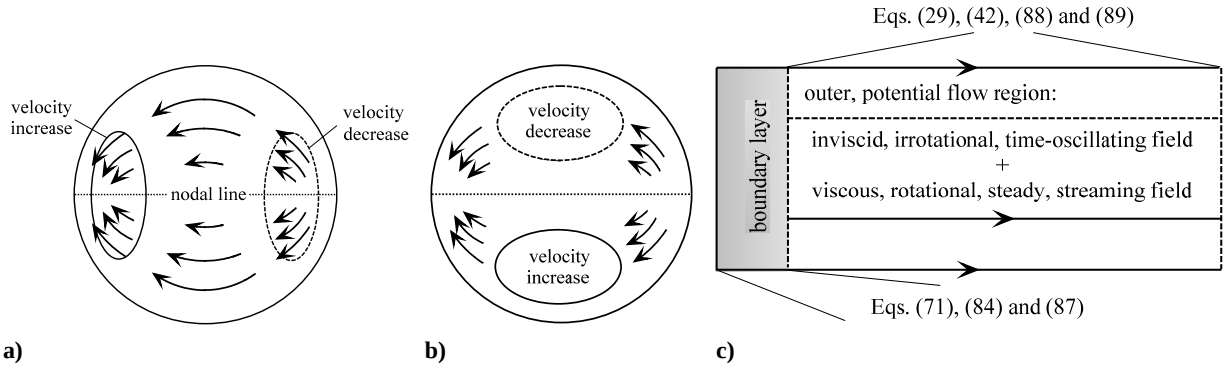

Figure 7. Sectors in which oscillatory waves are enhanced or weakened by virtue of streaming. These illustrate the outcome of interactions between a) radial and b) tangential velocities with the streaming motion. For example, in part a) the radially outward streaming contributions act to decelerate the radial wave in the right half while accelerating it in the left half. In part c) the main regions of interest are delineated along with their pertinent equations.

resulting from the use of a relatively sizable $\varepsilon = 0.1$. In stark contrast to Fig. 6b, no streaming consequences may be linked to Fig. 6c, where the viscous parameter is increased to $\delta = 0.0647$. At first glance, the diminishment in streaming intensity with successive increases in δ appears to be paradoxical, or perhaps counterintuitive, because secondary flows are rooted deep within the viscous boundary layer. Upon further scrutiny, however, one realizes that increasing δ leads to a smaller penetration number as expressed through Eq. (74). Decreasing S_p reduces, in turn, the boundary layer thickness or depth of penetration of the rotational segment through which streaming is generated. This inverse proportionality to δ is hoped to be expounded in forthcoming work.

In Fig. 7, three diagrams are provided to help visualize the key regions of interest. In Fig. 7a, we seek to isolate the coupling between streaming and radial waves. Being radially outward in all directions, streaming opposes the radial velocity waves in the right-hand-side sector of the domain, thus leading to a decreased local wave speed. By the same token, it enhances the radial wave in the left-hand-side sector, where it promotes further growth in the radial velocity. In Fig. 7b, the coupling with the tangential wave is examined. Given that streaming in the outer region is accompanied by small clockwise rotation (see Fig. 5c), its superposition on the counterclockwise motion of the tangential waves gives rise to regions with tangential velocity defect or excess, in the top and bottom halves of the domain, respectively. In practice, the coupling configurations shown in Figs. 7a and 7b occur simultaneously, thus leading to the patterns shown in Fig. 6b. Finally, to summarize the results obtained heretofore, Fig. 7c is used to delineate the main regions of interest and their pertinent solutions. For example, within the boundary layer region, the viscous treatment is most relevant. Applicable solutions include Eq. (71) for the first-order traveling wave solution and Eqs. (84)–(87) for the steady, second-order transverse velocities. In the outer region, the complete potential flow solution is depicted as the sum of the inviscid, irrotational, time-dependent field, given by Eqs. (29) and (42), and the viscous, rotational, steady streaming field given by Eqs. (88) and (89).

V. Conclusions

The present work investigates the secondary flows generated by parallel wave incidence over a uniformly injecting headwall. Of particular interest is how the streaming motion affects the oscillating field, especially in the tangential and radial directions. From the flow patterns depicted in Figs. 6 and 7, some interesting results may be inferred. Along the nodal pressure line (equator line in Fig. 6a), the flowfield is heavily dominated by radial velocities. Specifically, it is shown that along the nodal lines the flow is directed toward the center of the chamber on one side and out from the center on the other. Assuming that the velocity is proportional to the gradient of the pressure, a conclusion about the corresponding wave form may be inferred. In Fig. 6, the region where the velocity vectors are counterclockwise corresponds to a positive pressure region with the peak amplitude occurring along the outer circumference. Conversely, in the region where the flow is clockwise (down below the nodal line), a negative pressure region is formed with the troughs occurring along the outer circumference as well. Along the nodal line, where the velocity vectors converge or diverge, a transition from a positive to a negative pressure region is realized. We note that the second-order streaming flow for a traveling wave is axisymmetric, with a strong outward pointing radial component. Therefore, in the case where the secondary flow is large enough to influence the first-order oscillations, the radial coupling along the nodal line is affected the most. In the absence of streaming, an observer situated at the north or south poles (Fig. 6a) will witness the largest tangential velocities sweeping by. In the presence of streaming, the flow will no longer be tangential as it gains an outward pointing radial component near the poles (Fig. 6b). Along the equator line, the potential flow that is originally radial will be either enhanced or weakened downstream and upstream of the core, respectively. The result is a steepened wave form similar to that described by Pierce[38] in the case of a plane wave. It should be noted that as per Fig. 3, the secondary flow is one order of magnitude smaller than $\boldsymbol{u}^{(1)}$. Recalling that the problem is linearized by the ratio of the pressure fluctuations to the mean pressure, ε, terms at the second order in ε are quite small. This will remain true until the peak-to-peak amplitudes of the pressure oscillations become comparable to the chamber pressure, as reported in Clayton's data[18] and other experimental measurements taken in liquid rockets.

Our work clearly demonstrates the origination of streaming flows induced by tangential oscillations near a liquid rocket engine faceplate. Solutions to the first and second-order boundary layers are presented and discussed. The secondary flow patterns are found to increase the first-order pressure gradient in some areas and to decrease it in others. This process is associated with a steepening of the wave profile. Experimental evidence in the above discussion supports the development of a wave form that displays a sharp pressure spike followed by a long shallow trough. Our study calls for further investigations to relax some of the limiting assumptions used here. Since

tangential wave structures can steepen when interacting with an injector faceplate, a more elaborate model may be required to obtain a complete solution for the fully steepened waves.

Acknowledgments

This project was sponsored by the National Science Foundation and the University of Tennessee Space Institute.

References

[1]Hart, R. W., and McClure, F. T., "Combustion Instability: Acoustic Interaction with a Burning Propellant Surface," *The Journal of Chemical Physics*, Vol. 10, No. 6, 1959, pp. 1501-1514.

[2]Hart, R. W., and McClure, F. T., "Theory of Acoustic Instability in Solid Propellant Rocket Combustion," *Tenth Symposium (International) on Combustion*, 1964, pp. 1047-1066.

[3]Culick, F. E. C., "High Frequency Oscillations in Liquid Rockets," *AIAA Journal*, Vol. 1, No. 5, 1963, pp. 1097-1104.

[4]Culick, F. E. C., "Non-Linear Growth and Limiting Amplitude of Acoustic Oscillations in Combustion Chambers," *Combustion Science and Technology*, Vol. 3, No. 1, 1971, pp. 1-16.

[5]Flandro, G. A., "Theoretical Investigations of the Sergeant Roll Transient Problem," Sperry Utah Engineering Laboratory, Technical Rept. 211-SA-526C-61.14, Salt Lake City, April 1961.

[6]Flandro, G. A., "On Flow Turning," AIAA Paper 95-2530, July 1995.

[7]Flandro, G. A., and Sotter, J. G., "Unstable Combustion in Rockets," *Scientific American*, 1968.

[8]Flandro, G. A., Majdalani, J., and Sims, J. D., "Nonlinear Longitudinal Mode Instability in Liquid Propellant Rocket Engine Preburners," AIAA Paper 2004-4162, July 2004.

[9]Flandro, G. A., Majdalani, J., and Sims, J. D., "On Nonlinear Combustion Instability in Liquid Propellant Rocket Engines," AIAA Paper 2004-3516, July 2004.

[10]Fischbach, S. R., Majdalani, J., and Flandro, G. A., "Acoustic Instability of the Slab Rocket Motor," *Journal of Propulsion and Power*, Vol. 23, No. 1, 2007, pp. 146-157.

[11]Fischbach, S. R., Majdalani, J., and Flandro, G. A., "Verification and Validation of Rocket Stability Integral Transformations," AIAA Paper 2005-4001, July 2005.

[12]Fischbach, S. R., Majdalani, J., and Flandro, G. A., "Acoustic Instability of the Slab Rocket Motor," AIAA Paper 2004-4061, July 2004.

[13]Fischbach, S. R., Flandro, G. A., and Majdalani, J., "Volume-to-Surface Transformations of Rocket Stability Integrals," AIAA Paper 2004-4053, July 2004.

[14]Flandro, G. A., and Majdalani, J., "Aeroacoustic Instability in Rockets," *AIAA Journal*, Vol. 41, No. 3, 2003, pp. 485-497.

[15]Fabignon, Y., Dupays, J., Avalon, G., Vuillot, F., Lupoglazoff, N., Casalis, G., and Prévost, M., "Instabilities and Pressure Oscillations in Solid Rocket Motors," *Journal of Aerospace Science and Technology*, Vol. 7, No. 3, 2003, pp. 191-200.

[16]Ugurtas, B., Avalon, G., Lupoglazoff, N., Vuillot, F., and Casalis, G., "Stability and Acoustic Resonance of Internal Flows Generated by Side Injection," *Solid Propellant Chemistry, Combustion, and Motor Interior Ballistics*, Vol. 185, edited by V. Yang, T. B. Brill, and W.-Z. Ren, AIAA Progress in Astronautics and Aeronautics, Washington, DC, 2000, pp. 823-836.

[17]Majdalani, J., Flandro, G. A., and Fischbach, S. R., "Some Rotational Corrections to the Acoustic Energy Equation in Injection-Driven Enclosures," *Physics of Fluids*, Vol. 17, No. 7, 2005, pp. 0741021-20.

[18]Clayton, R. M., "Experimental Measurements on Rotating Detonation-Like Combustion," JPL, Technical Rept. 32-788, Pasadena, CA, August 1965.

[19]Clayton, R. M., Rogero, R. S., and Sotter, J. G., "An Experimental Description of Destructive Liquid Rocket Resonant Combustion," *AIAA Journal*, Vol. 6, No. 7, 1968, pp. 1252-1259.

[20]Sotter, J. G., Woodward, J. W., and Clayton, R. M., "Injector Response to Strong High-Frequency Pressure Oscillations," *Journal of Spacecraft and Rockets*, Vol. 6, No. 4, 1969, pp. 504-506.

[21]Sotter, J. G., and Clayton, R. M., "Monitoring the Combustion Process in Large Engines," *Journal of Spacecraft and Rockets*, Vol. 4, No. 5, 1967, pp. 702-703.

[22]Maslen, S. H., and Moore, F. K., "On Strong Transverse Waves without Shocks in a Circular Cylinder," *Journal of the Aeronautical Sciences*, Vol. 23, 1956, pp. 583-593.

[23]Flandro, G. A., "Rotating Flows in Acoustically Unstable Rocket Motors," Ph.D. Dissertation, California Institute of Technology, 1967.

[24]Majdalani, J., "Improved Flowfield Models in Rocket Motors and the Stokes Layer with Sidewall Injection," Ph.D. Dissertation, University of Utah, 1995.

[25]Majdalani, J., "Characterization of the Laminar Boundary Layer in Solid Rocket Motors," AIAA Paper 98-3699, July 1998.

[26]Majdalani, J., and Van Moorhem, W. K., "Improved Time-Dependent Flowfield Solution for Solid Rocket Motors," *AIAA Journal,* Vol. 36, No. 2, 1998, pp. 241-248.

[27]Majdalani, J., "The Boundary Layer Structure in Cylindrical Rocket Motors," *AIAA Journal,* Vol. 37, No. 4, 1999, pp. 505-508.

[28]Majdalani, J., and Flandro, G. A., "The Oscillatory Pipe Flow with Arbitrary Wall Injection," *Proceedings of the Royal Society, London, Series A,* Vol. 458, No. 2022, 2002, pp. 1621-1651.

[29]Jankowski, T. A., and Majdalani, J., "Vortical and Acoustical Mode Coupling inside a Porous Tube with Uniform Wall Suction," *Journal of the Acoustical Society of America,* Vol. 117, No. 6, 2005, pp. 3448-3458.

[30]Schlichting, H., *Boundary-Layer Theory*, 7th ed., McGraw-Hill, New York, 1979.

[31]Westervelt, P. J., "The Theory of Steady Rotational Flow Generated by a Sound Field," *The Journal Of The Acoustical Society Of America,* Vol. 25, No. 1, 1953, pp. 60-67.

[32]Nyborg, W. L., "Acoustic Streaming Due to Attenuated Plane Waves," *Journal of the Acoustical Society of America,* Vol. 25, No. 1, 1953, pp. 68-75.

[33]Cole, J. D., and Aroesty, J., "The Blowhard Problem-Inviscid Flows with Surface Injection," *International Journal of Heat and Mass Transfer,* Vol. 11, No. 7, 1968, pp. 1167-1183.

[34]Majdalani, J., "A Hybrid Multiple Scale Procedure for Boundary Layers Involving Several Dissimilar Scales," *Journal of Applied Mathematics and Physics (ZAMP),* Vol. 49, No. 6, 1998, pp. 849-868.

[35]Majdalani, J., "Asymptotic Formulation for an Acoustically Driven Field inside a Rectangular Cavity with a Well-Defined Convective Mean Flow Motion," *Journal of Sound and Vibration,* Vol. 223, No. 1, 1999, pp. 73-95.

[36]Majdalani, J., and Roh, T. S., "The Oscillatory Channel Flow with Large Wall Injection," *Proceedings of the Royal Society, London, Series A,* Vol. 456, No. 1999, 2000, pp. 1625-1657.

[37]Majdalani, J., "The Oscillatory Channel Flow with Arbitrary Wall Injection," *Journal of Applied Mathematics and Physics (ZAMP),* Vol. 52, No. 1, 2001, pp. 33-61.

[38]Pierce, A. D., *Acoustics, an Introduction to Its Physical Principles and Applications*, Acoustical Society of America, New York, 1989.